

Disassembling the Galaxy with angle-action coordinates

Paul J. McMillan^{*}, and James J. Binney

Rudolf Peierls Centre for Theoretical Physics, 1 Keble Road, Oxford, OX1 3NP, UK

26 October 2018

ABSTRACT

Angle-action coordinates are used to study the relic of an N -body simulation of a self-gravitating satellite galaxy that was released on a short-period orbit within the disc of the Galaxy. Satellite stars that lie within 1.5 kpc of the Sun are confined to a grid of patches in action space. As the relic phase-mixes for longer, the patches become smaller and more numerous. These patches can be seen even when the angle-action coordinates of an erroneous Galactic potential are used, but using the wrong potential displaces them. Diagnostic quantities constructed from the angle coordinates both allow the true potential to be identified, and the relic to be dated. Hence when the full phase space coordinates of large numbers of solar-neighbourhood stars are known, it should be possible to identify members of particular relics from the distribution of stars in an approximate action space. This would then open up the possibility of determining the time since the relic was disrupted and gaining better knowledge of the Galactic potential.

The availability of angle-action coordinates for arbitrary potentials is the key to these developments. The paper includes a brief introduction to the torus technique used to generate them.

Key words: methods: numerical – Galaxy: kinematics and dynamics – Galaxy: structure – solar neighbourhood

1 INTRODUCTION

Within the remarkably successful Λ CDM model, galaxy formation is a hierarchical process. Large galaxies, such as the Milky Way, are built up in mergers and the accretion of smaller building blocks (e.g. White & Rees 1978; Springel & Hernquist 2003). The signatures of these processes should still be visible today in the form of substructure such as streams in all components of the Milky Way (e.g. Lynden-Bell & Lynden-Bell 1995; Freeman & Bland-Hawthorn 2002; Helmi et al. 2003; Abadi et al. 2003).

Evidence of the wealth of substructure in the stellar halo of the Milky Way has increased dramatically over the past 15 years, most notably with observations of the disrupting Sagittarius dwarf galaxy (Ibata et al. 1994), and of the streams visible in the SDSS data (e.g. Belokurov et al. 2006). Within the disc several substructures are known, as are several mechanisms that might be responsible for them. Stars are born in clusters within the disc, and over a period of several Galactic rotations these clusters evaporate and the stars become phase mixed, spreading in space but retaining closely related orbits. This is commonly referred to

as a supercluster – it is likely the Hyades-Pleiades supercluster formed this way (Famaey et al. 2005). Substructure can also be created by dynamical interaction with spiral arms, or a rotating bar component; for example the Hercules stream is thought to be associated with the bar of the Milky Way (Dehnen 1999, 2000; Fux 2001). It has been suggested that the Arcturus group (Eggen 1971) is debris from a merged satellite (Navarro et al. 2004).

Many methods exist for finding this substructure, often based on incomplete phase space information about the stars. In the outer parts of the halo it is possible to find substructure with only knowledge of stellar positions on the sky, sometimes in conjunction with photometric data (e.g. Belokurov et al. 2006), or radial velocity measurements (e.g. Lynden-Bell & Lynden-Bell 1995; Helmi & White 1999). In the solar neighbourhood, approaches that look for common proper motions have been widely used, (e.g. Chereul et al. 1999).

With the availability of full 6D phase space information for an increasing number of stars in the solar neighbourhood, most notably the catalogues resulting from the Geneva-Copenhagen and RAVE surveys (Nordström et al. 2004; Steinmetz et al. 2006; Zwitter et al. 2008), and with the prospect of a further increase by several orders of magnitude when Gaia data become available (Perryman et al.

^{*} E-mail: p.mcmillan1@physics.ox.ac.uk

2001), it is appropriate to consider methods for using these data in full.

As discussed in Helmi et al. (1999), the space of integrals of motion is a very promising one for finding substructure such as superclusters or merger debris. Stars with a single small progenitor (star cluster or small galaxy) will have very similar values for the integrals, which will ensure they are tightly bunched in integral space even after phase mixing has produced a spatial distribution that is effectively featureless. There are additional benefits to using quantities that are not only integrals but adiabatic invariants, as these are more likely to remain constant as the Galactic potential changes over time.

Previous work has focused on spaces defined by L_z (which is an adiabatic invariant in an axisymmetric potential), and other quantities that can be used as approximate integrals of the motion, such as the total angular momentum (only an integral of the motion in a spherically symmetric potential, Helmi et al. 1999), or are not adiabatic invariants, such as the energy (Helmi & de Zeeuw 2000) or the apocentre and pericentre of an orbit (Helmi et al. 2006).

In this paper we demonstrate the use of angle-action coordinates to find substructure in the solar neighbourhood. Actions are adiabatic invariants, and their conjugate variables, the ‘‘angle coordinates’’, increase linearly in time. As Tremaine (1999) has pointed out, these properties make them exceptionally useful for analysing tidal streams. The difficulty of determining the actions of stars in non-spherical potentials has, however, severely restricted their application to date. This is the first in a series of papers in which we show how the concept of orbital tori (McGill & Binney 1990; Kaasalainen & Binney 1994) makes it possible to exploit the power of angle-action coordinates for practical galactic problems.

In Sections 2 & 3 we briefly introduce angle-action coordinates, and explain how we find them for stars with known phase space positions. In Section 4 we apply them to simulated data of a satellite merger. We show that stars from the satellite that are observed in the solar neighbourhood are confined to a grid of patches in action space, even when rather a poor approximation to the Galactic potential is used. We show further that a diagnostic defined in terms of the angle coordinates enables the true potential to be distinguished from the false one. Section 5 discusses minor modifications to the analysis that are required to accommodate secular evolution of the Galactic potential over the life of a relic.

2 ANGLE-ACTION COORDINATES

Three actions J_i and three conjugate angles coordinates θ_i provide canonical coordinates for six-dimensional phase space (e.g. Binney & Tremaine 2008, §3.5). The conventional phase space coordinates $\mathbf{w} \equiv (\mathbf{x}, \mathbf{v})$ are 2π -periodic in the angles. The actions are conserved quantities for any orbit, and the angles increase linearly with time:

$$\boldsymbol{\theta}(t) = \boldsymbol{\theta}(0) + \boldsymbol{\Omega}(\mathbf{J})t, \quad (1)$$

where the components of $\boldsymbol{\Omega}$ are the orbital frequencies. Thus, in six-dimensional $(\boldsymbol{\theta}, \mathbf{J})$ space, a bound orbit moves only in the three θ_i directions, over a surface that is topologically a

three-dimensional torus. We generally refer to this model of the orbit as ‘‘the torus’’; it is labelled by the actions \mathbf{J} .

Angle-action coordinates exist for any time-independent, integrable Hamiltonian. However, an analytic method of computing the transformations between normal phase space coordinates and angle-action coordinates $\mathbf{w} \leftrightarrow (\boldsymbol{\theta}, \mathbf{J})$ is only practical for the Hamiltonian defined by the isochrone potential, which as limiting cases includes the harmonic-oscillator and Kepler potentials (Binney & Tremaine 2008, §3.5.2).

The Hamiltonian corresponding to a more realistic galaxy potential is not generally integrable. However, most orbits in an axisymmetric potential are approximately ‘regular’ (non-chaotic), and thus admit three approximate isolating integrals of motion. Consequently, it is possible to find angle-action coordinates which describe motion on these orbits over all interesting time-scales.

Methods for constructing angle-action tori for orbits in a general potential have been in the literature for over a decade (McGill & Binney 1990; Kaasalainen & Binney 1994), but have been little utilised, primarily because of the technical challenges these methods present. It is, however, possible to encapsulate these technicalities so that users are protected from them, and once this has been done, it is nearly as easy to construct angle-action coordinates for an orbit in an axisymmetric potential as it is to numerically integrate the orbit with a Runge-Kutta routine, or similar.

2.1 The torus method

In our current implementation we restrict ourselves to orbits in axisymmetric potentials. Conservation of angular momentum, J_ϕ , about the system’s symmetry axis then reduces the problem to that of motion in the (R, z) meridional plane in the effective potential $\Phi_{\text{eff}}(R, z) \equiv \Phi(R, z) + J_\phi^2/2R^2$ (e.g. Binney & Tremaine 2008, §3.2). J_ϕ is the third action.

We start with a ‘toy’ Hamiltonian, H^T , for which the relationship $(R, z, p_R, p_z) \leftrightarrow (\theta_R^T, \theta_z^T, J_R^T, J_z^T)$ is known analytically,¹ namely that of a generalised effective isochrone potential

$$\Phi_{\text{eff}}^T(r, \vartheta) = \frac{-GM}{b + \sqrt{b^2 + (r - r_0)^2}} + \frac{L_z^2}{2[(r - r_0) \sin \vartheta]^2}, \quad (2)$$

where ϑ is latitude (not to be confused with the dynamical angle coordinates); M , b , L_z and r_0 are free parameters of the toy Hamiltonian.

As described in detail in McGill & Binney (1990), the toy torus $\mathbf{J}^T = \text{constant}$ is distorted into the ‘target torus’ that approximates the orbit by the generating function

$$S(\boldsymbol{\theta}^T, \mathbf{J}) = \boldsymbol{\theta}^T \cdot \mathbf{J} + 2 \sum_{\mathbf{n} > 0} S_{\mathbf{n}}(\mathbf{J}) \sin(\mathbf{n} \cdot \boldsymbol{\theta}^T), \quad (3)$$

where \mathbf{n} is a two-vector with integer components and the

¹ In this paper we refer to variables such as the angles and actions in the toy Hamiltonian as $\boldsymbol{\theta}^T, \mathbf{J}^T$, and those in the target Hamiltonian as $\boldsymbol{\theta}, \mathbf{J}$. This notation differs from that of McGill & Binney (1990) and Kaasalainen & Binney (1994), in which the *toy* angles and actions are referred to as $\boldsymbol{\theta}, \mathbf{J}$, and those in the target potential as $\boldsymbol{\theta}', \mathbf{J}'$. We make this change in notation as our focus is primarily on the *application* of this machinery, rather than on how it works.

notation $\mathbf{n} > 0$ indicates that the sum runs over exactly half the plane, with the origin excluded. The $S_{\mathbf{n}}$ are free parameters of the generating function. The canonical transformation defined by this generating function is

$$\mathbf{J}^T = \frac{\partial S(\boldsymbol{\theta}^T, \mathbf{J})}{\partial \boldsymbol{\theta}^T} ; \quad \boldsymbol{\theta} = \frac{\partial S(\boldsymbol{\theta}^T, \mathbf{J})}{\partial \mathbf{J}}. \quad (4)$$

so

$$\mathbf{J}^T = \mathbf{J} + 2 \sum_{\mathbf{n}>0} \mathbf{n} S_{\mathbf{n}}(\mathbf{J}) \cos(\mathbf{n} \cdot \boldsymbol{\theta}^T) \quad (5)$$

$$\boldsymbol{\theta} = \boldsymbol{\theta}^T + 2 \sum_{\mathbf{n}>0} \frac{\partial S_{\mathbf{n}}(\mathbf{J})}{\partial \mathbf{J}} \sin(\mathbf{n} \cdot \boldsymbol{\theta}^T). \quad (6)$$

Since the transform is canonical for any values $S_{\mathbf{n}}$, and the toy torus is “null” in the sense that Poincaré’s integral $\int_A d\mathbf{p} \cdot d\mathbf{q}$ vanishes for any region A of the torus, the image of the toy torus under the canonical map (the target torus) is also null. Note that \mathbf{J} is constant on the target torus, so in general \mathbf{J}^T is a non-trivial function of $\boldsymbol{\theta}^T$.

The values $S_{\mathbf{n}}(\mathbf{J})$ (and the parameters of H^T) corresponding to a given gravitational potential and \mathbf{J} are found by enforcing the condition that the Hamiltonian H is constant on the target torus. Remarkably this condition is sufficient to ensure that the torus corresponds to an orbit in the given galaxy potential. In practice we enforce this condition by using the Levenberg-Marquardt algorithm (e.g. Press et al. 1986) to minimize the statistic $\chi^2 = \frac{1}{N_p} \sum (H - \bar{H})^2$, where the sum is over N_p points spread evenly in $\boldsymbol{\theta}^T$ over the target torus. The derivatives of H with respect to the $S_{\mathbf{n}}$ and the parameters of the toy Hamiltonian that the Levenberg-Marquardt algorithm requires can all be found through the chain rule. We generally refer to this process as an “action fit”.

This minimisation determines the functional dependence $\mathbf{w}(\boldsymbol{\theta}^T, \mathbf{J})$. However, it does not tell us how \mathbf{w} depends on $\boldsymbol{\theta}$: the $S_{\mathbf{n}}$ have been determined for a single value of \mathbf{J} , so $\partial S_{\mathbf{n}}(\mathbf{J})/\partial \mathbf{J}$ is still undetermined. It is, however, possible to find *approximate* values for the frequencies, $\boldsymbol{\Omega}$, by performing an orbit integration over several periods in the target potential, starting from a phase space point on the torus, and performing a linear fit to the resulting values of $\theta_i^T(t)$.

To find more accurate frequencies and expressions for the angle coordinates, we integrate small sections of the orbit, starting from a grid of points on the torus, and use the equations (Kaasalainen & Binney 1994)

$$\boldsymbol{\theta}(0) + \boldsymbol{\Omega}t = \boldsymbol{\theta}^T(t) + 2 \sum_{\mathbf{n}>0} \frac{\partial S_{\mathbf{n}}(\mathbf{J})}{\partial \mathbf{J}} \sin[\mathbf{n} \cdot \boldsymbol{\theta}^T(t)]. \quad (7)$$

Each integration for M time-steps yields $3M$ such equations in which $\boldsymbol{\theta}(0)$, $\boldsymbol{\Omega}$, and $\partial S_{\mathbf{n}}(\mathbf{J})/\partial \mathbf{J}$ are unknowns. The equations are linear in the unknowns and for $M \gg 1$ the number of available equations increases much faster than the number of unknowns. We truncate the sum over \mathbf{n} to ensure that the number of unknowns is significantly less than the number of equations, and solve the equations using a least squares fit. We refer to this process as an “angle fit”.

3 FITTING THE DATA

The torus-fitting mechanism enables us to find $\mathbf{w}(\boldsymbol{\theta}, \mathbf{J})$ for given values of \mathbf{J} rather than enabling us to determine $(\boldsymbol{\theta}, \mathbf{J})$

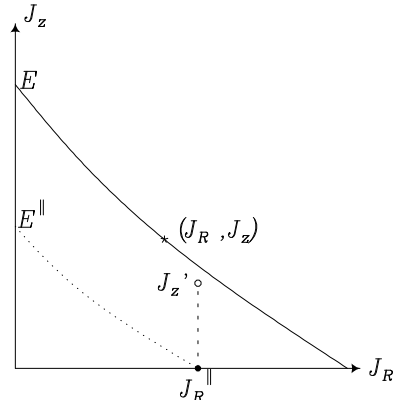


Figure 1. Iterative procedure for determining $\mathbf{J}(\mathbf{w})$. We start by evaluating the planar orbit with energy E^{\parallel} (black dot). From its radial action and vertical frequency we move to the open circle $(J_R^{\parallel}, J_z^{\parallel})$. Further vertical moves are used to reach the line on which the energy is that of the star. Then we move along that line to the star, where the velocities of the orbit agree with those of the star.

given the coordinates \mathbf{w} of a star. We now explain how we go from \mathbf{w} to $(\boldsymbol{\theta}, \mathbf{J})$ by an iterative procedure, which is somewhat ad-hoc, but converges quickly. We have the numerical value L_z of J_ϕ , so the problem is to find a point in the slice through action space $J_\phi = L_z$. Fig. 1 shows this slice. Several lines of constant H are shown: the full line is the line that corresponds to the energy E of the given star. The dotted line is for the “planar energy” $E^{\parallel} \equiv \frac{1}{2}v_R^2 + \Phi_{\text{eff}}(R, 0)$ that the star would have if it were confined to the Galactic plane. Simple one-dimensional integrals enable us to find the action J_R^{\parallel} and time-averaged radius \bar{R} of the orbit represented by the intersection of the dotted line with the J_R axis. Our iterations start at this point, as J_R^{\parallel} is typically a good estimate for the true value of J_R .

From there we move vertically up towards the full line by an amount J_z' . Bearing in mind that $\Omega_z = \partial H/\partial J_z$, we estimate J_z' from the first-order expression $E \simeq H(J_R^{\parallel}, J_z) \simeq E^{\parallel} + \Omega_z J_z'$. That is, we take $J_z' = (E - E^{\parallel})/\nu_{\bar{R}}$, where we have approximated Ω_z by the vertical epicycle frequency ν at \bar{R} .

We obtain the torus $(J_R^{\parallel}, J_z', L_z)$ and using its energy E_2 and frequency Ω_z we obtain an improved approximation to J_z by incrementing J_z' by $\Delta J_z' = (E - E_2)/\Omega_z$. This step is repeated until the energy of the current torus is sufficiently close to E .

Once we have converged onto the line $H = E$ in Fig. 1, we can move along it with increments $\Delta \mathbf{J}$ to \mathbf{J} that satisfy (to first order) $\boldsymbol{\Omega} \cdot \Delta \mathbf{J} = 0$ – in this process only the R and z components of \mathbf{J} are changing, so $\Delta \mathbf{J}$ is determined by ΔJ_z .

If the orbit does not go through the location of the star, ΔJ_z is increased when the maximum height at the star’s radius is too small, and decreased when the orbit does not reach the star’s radius. Once the orbit reaches the star, J_z is adjusted until the local value of v_z agrees with the observational value.

This procedure has converged for all values of \mathbf{J} that we have tried, (irrespective of, for example, whether J_z is small) and typically involves ~ 20 torus fits per star. With our current torus-finding code (which we have not attempted

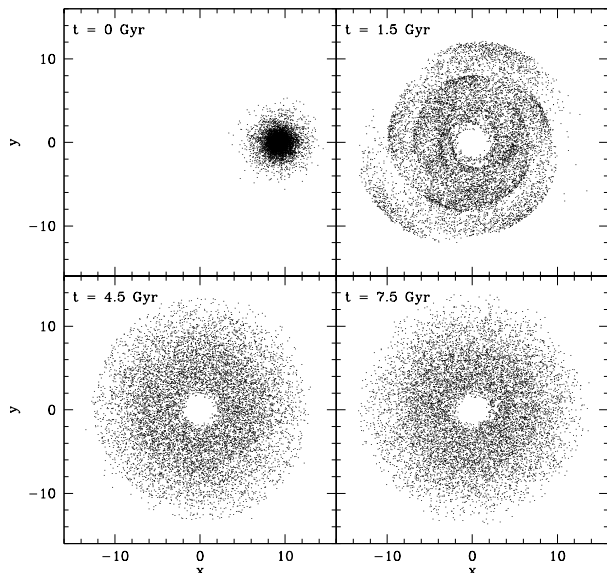


Figure 2. Particle positions in the x - y (Galactic) plane initially and after $t = 1.5, 4.5$ and 7.5 Gyr (as labelled).

to optimize for speed) the procedure requires ~ 15 s per star, so even now actions could be found for tens of millions of stars in of order a week on a cluster of 1000 processors.

After fitting a torus to the observations, we obtain the star’s angle coordinates and more accurate frequency values by performing an angle fit.

4 APPLICATION TO SIMULATION DATA

To illustrate what can be achieved with the torus method, we use it to examine the debris of a self-gravitating satellite that was disrupted during an N -body simulation in which the satellite moved in a fixed Galactic potential. We focus on a case that is very similar to that described in Section 3.2 of Helmi et al. (2006), which was designed to reproduce the properties of the Arcturus group.

We represented the satellite by 5×10^5 particles in a King sphere of concentration $c = \log_{10}(r_i/r_c) = 1.25$, core radius 0.39 kpc, and total mass $3.75 \times 10^8 M_\odot$. It was placed on an orbit in the plane of the Galaxy that has apocentre at 9.3 kpc, pericentre at 3.1 kpc, and angular momentum 970 kpc km s $^{-1}$. The satellite is initially placed at apocentre and followed for ~ 9 Gyr.

The self-gravity of the satellite was found using GYRFALCON (Dehnen 2002) and the static Galaxy potential was that of Model 2 in Dehnen & Binney (1998). This model is axisymmetric, and consists of somewhat flattened spheroids representing the halo and bulge, and three exponential disc components to represent the gas disc and the thin and thick stellar discs.

The particle positions in the x - y plane are plotted in Figure 2 for the initial conditions and at $t = 1.5, 4.5$ and 7.5 Gyr. After 1.5 Gyr the satellite is spread over all azimuths and particles are found over their entire radial range, but substructure is clearly visible. After 4.5 Gyr phase mixing

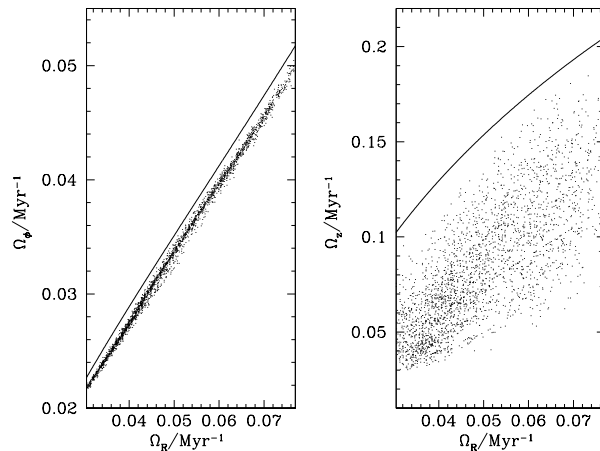


Figure 3. Ω_ϕ (left) and Ω_z (right) plotted against Ω_R for a random sample of particles from our simulation. The lines shows the the rotational frequency of a circular orbit Ω_{circ} (left) and vertical frequency ν (right) plotted against the epicycle frequency κ .

has progressed to the extent that this structure is nearly undetectable from the physical positions alone.

We calculated angles, actions and frequencies for satellite particles using both the true potential and a rather different potential – a Miyamoto-Nagai potential (Section 4.3).

4.1 The frequencies

Fig. 3 shows a random sample of satellite particles at $t = 9$ Gyr in the (Ω_ϕ, Ω_R) plane (left) and the (Ω_z, Ω_R) plane (right) when the true potential is used. The full lines show the relationship between the epicycle frequency $\kappa \simeq \Omega_R$ and the circular frequency $\Omega_{\text{circ}} \simeq \Omega_\phi$ (left) or vertical frequency $\nu \sim \Omega_z$ (right). These demonstrate that the strong correlation between Ω_R and Ω_ϕ arises because each frequency depends strongly on energy and only much more weakly on either eccentricity or inclination to the plane. The relationship between Ω_z and the other frequencies is much broader, reflecting the strongly anharmonic nature of vertical oscillations, which cause the vertical frequency to depend strongly on vertical amplitude. Because the simulated satellite is on an orbit in the Galactic plane, Ω_z is of little further interest in this study (though it will be in other cases).

Consider now the frequencies of particles that lie in a given volume around the Sun, as survey stars usually do. We place the Sun 8 kpc from the Galactic centre along the line to the satellite’s initial location and select particles that lie within 1.5 kpc of the Sun. Fig. 4 shows these stars at $t = 1.5, 4.5$ and 7.5 Gyr in the plane spanned by $\Omega_\phi t/2\pi$ and $\Omega_R t/2\pi$ – the number of rotations about the galactic centre and the number of radial periods, respectively. Now we see a clear substructure within the plot. Stars are found in patches at (close to) integer intervals in $\Omega_\phi t/2\pi$, and regularly in $\Omega_R t/2\pi$.

The reason for this clumping is simple: to be in the solar neighbourhood at time t , having also all been near each other at an earlier point in time (when part of a single satellite), these particles must all have moved a certain amount in ϕ , plus or minus an integer number of complete rotations

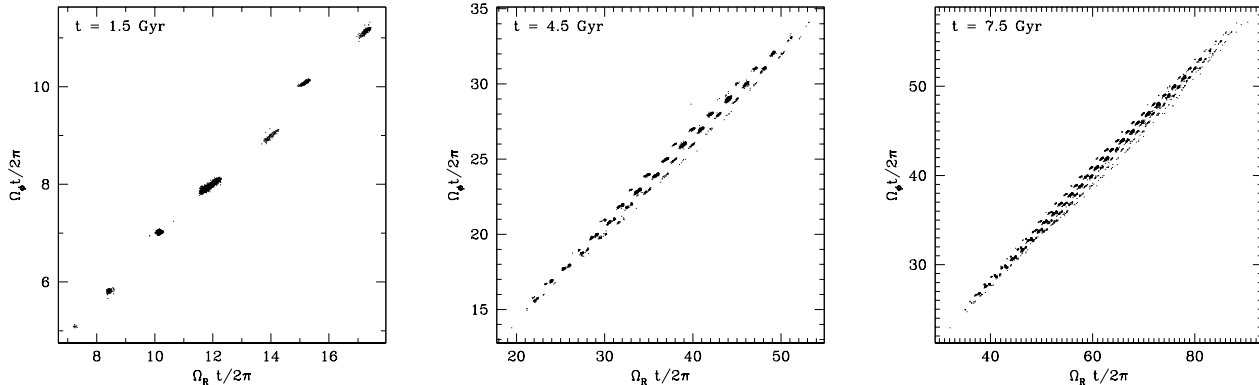


Figure 4. $\Omega_\phi t/2\pi$ (number of azimuthal periods) plotted against $\Omega_R t/2\pi$ (number of radial periods) for particles within 1.5 kpc of the “solar position” in our simulation after 1.5, 4.5 and 7.5 Gyr (left to right). The particles are separated into patches corresponding to those particles which have performed (approximately) an integer number of rotations about the Galactic centre, and are at the appropriate point in their radial oscillations.

about the Galactic Centre. This is, in essence, a selection effect caused by taking a window of finite size. Even after 7.5 Gyr, at which point phase mixing has rendered the spatial distribution essentially featureless (Figure 2), there is manifest clumping in the Ω plot. In the case of $\Omega_R t/2\pi$ the patches occur more frequently than at integer intervals because the orbits cross the radial range twice per radial period. The non-zero size of the patches reflects the non-zero size of the window, non-zero initial velocities of the particles relative to the satellite motion and the non-negligible mass of the satellite, which causes orbits to deviate from orbits in the Galactic potential at early times. There is also a small spread due to any errors in the value of Ω found – this is clearly a small effect as the patches are still distinct after 7.5 Gyr. The spread in Ω_z among stars in these samples is no narrower than that of all the satellite’s stars, and not separated into patches, both because our window constrains z only weakly, and because the initial values of θ_z range from zero to 2π as a result of the satellite starting from the plane with $v_z = 0$.

The number of patches in Ω -space increases approximately as t^2 , since the number of integers that lie in the full range of $\Omega_R t/2\pi$ or $\Omega_\phi t/2\pi$ is proportional to t (since the range of Ω doesn’t change). The size of individual patches is, to a first approximation, determined by the size of the window from which particles are chosen: if an orbit lies within the window over a range $\Delta\theta_R$ (ignoring for simplicity the dependence on θ_z, θ_ϕ), then in Ω -space (as opposed to $\Omega t/2\pi$ -space) each individual patch will have width $\Delta\theta_R/t$. Therefore the size of each patch in Ω -space is proportional to t^{-2} , so the total area of the patches is approximately time-independent. The other effects mentioned above that cause the patches to have finite size have a similar effect on the size of the patches with the exception of the error in measurements of Ω . Some of the patches are restricted in size because they meet the edge of the envelope of available Ω -values (the values found in the satellite as a whole – Figure 3, left). This is probably most obvious in the left panel of Figure 4, in which one patch (at $\Omega_\phi t/2\pi = 8$) is far larger than the others because it nowhere touches the envelope.

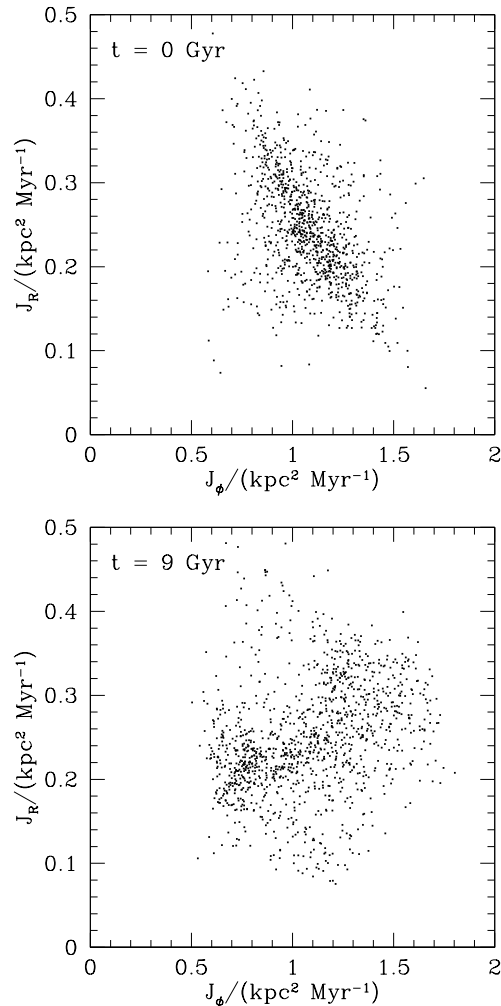


Figure 5. J_R plotted against J_ϕ for a random sample of particles at the beginning of the simulation (top) and after 9 Gyr of evolution (bottom).

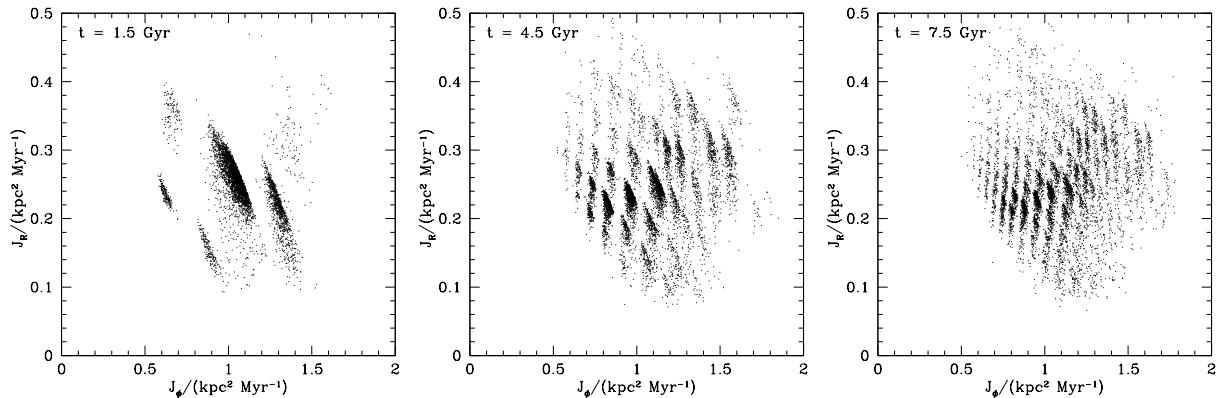


Figure 6. J_R plotted against J_ϕ for particles within 1.5 kpc of the “solar position” in our simulation after 1.5, 4.5 and 7.5 Gyr (left to right). As in Figure 4, the particles are divided into patches which increase in number and decrease in size as t increase.

4.2 The actions

Helmi et al. (2006) sought to identify substructure in the disc by calculating the locations of stars in “APL” space, which is the space spanned by apocentre, pericentre and J_ϕ (which they refer to as L_z). Apo- and pericentre can be considered to be integrals analogous to actions, so APL space is a mapping of action space. Hence it is of interest to examine the distribution of the satellite’s stars in action space for comparison with the results of Helmi et al. (2006) although we shall find it less interesting than the frequency and angle spaces.

Fig. 5 is a plot of J_R against J_ϕ for a random set of particles (reflecting the satellite as a whole) at the beginning of the simulation (top) and at $t = 9$ Gyr (bottom). The particles remain in the same general area of the (J_ϕ, J_R) plane, but at early times the actions are not constant because the satellite is self-gravitating and the strong negative correlation between J_R and J_ϕ seen in the initial conditions is replaced by a (rather weaker) positive correlation.²

The strong negative correlation in the initial conditions arises because initially the satellite is at apocentre. A particle that moves relative to the centre of the satellite in the opposite direction to the satellite’s rotation about the Galactic centre has less angular momentum than one that moves in the opposite direction, and – in the absence of the satellite’s self-gravity – would be on a more eccentric orbit, and thus have a higher value of J_R .

The weaker correlation between J_R and J_ϕ seen at 9 Gyr arises because the actions of a particle become constant when the particle is stripped from the satellite and starts to feel the latter’s gravity only weakly. This occurs at pericentre, when the effect of combining motion within the satellite with the motion of the satellite is precisely opposite of what it is at apocentre. The extent of the correlation between J_R and J_ϕ at 9 Gyr is comparable to that shown in Fig. 5 of Helmi et al. (2006) for the locations in APL space of stars that lie within 5 kpc of the Sun.

Figure 6 is a plot of J_R against J_ϕ for particles that lie within 1.5 kpc of the Sun at $t = 1.5, 4.5$ and 7.5 Gyr

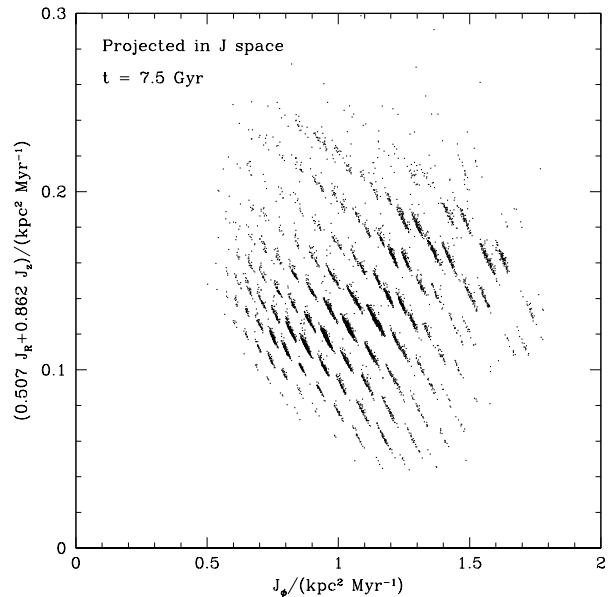


Figure 7. A projection in \mathbf{J} space of the actions of particles within 1.5 kpc of the “solar position” in the simulation after 7.5 Gyr (the same particles plotted in Figure 6, right). In this projection it is clearer that the stars are separated into individual clumps in \mathbf{J} space.

(left to right). The actions of the particles found in the solar neighbourhood cover almost the entire range in \mathbf{J} found in the satellite as a whole, but are separated into distinct patches that decrease in size and increase in number over time. The number of patches increases slightly faster than the area of each patch decreases with the result that by 7.5 Gyr the patches are starting to merge into bands. Fig. 5 of Helmi et al. (2006) shows such a series of bands in APL space for stars that lie within 1.5 kpc of the Sun.

Since Ω is a smooth function of \mathbf{J} , our study of the distribution of particles in frequency space explains their distribution in action space: the “allowed” values of \mathbf{J} correspond to “allowed” values of Ω , which are confined to patches. While the constraints on Ω do not involve Ω_z , the constraints on \mathbf{J} do depend on J_z , because both Ω_R and Ω_ϕ

² When the satellite’s self-gravity is turned off, the actions prove to be constant as expected.

depend on J_z . Consequently, the positions of stars in \mathbf{J} -space form a relatively regular lattice, but the principal directions of that lattice are not parallel to the J_i axes. Therefore, the tendency of patches to run together in the extreme right-hand panel of Fig. 6 can be eliminated by plotting a different projection of action space. For example, Figure 7 is a plot of $0.507J_R + 0.862J_z$ against J_ϕ – a projection chosen by eye from a 3D visualisation of the distribution in \mathbf{J} -space – and in this plot the patches are all distinct. In general, the patches will be most cleanly separated when the lattice is projected along one of its principal directions, since then points with the same Ω_R and Ω_ϕ but differing in Ω_z are projected on top of one another. The optimum projection depends both on the potential and on the region of \mathbf{J} -space occupied by the stars, but it can be straightforwardly identified for any set of data because $\mathbf{\Omega}$ is found at the same time as \mathbf{J} .

4.3 Working with incomplete knowledge

In reality we do not know the Galaxy’s potential a priori. In this subsection we show that satellite particles can be identified using even a poor approximation to the potential, and then the true potential identified from structure within the sample of satellite particles.

We repeated the above analysis using orbital tori in the Hamiltonian for a Miyamoto-Nagai potential

$$\Phi_{\text{MN}}(R, z) = -\frac{GM}{\sqrt{R^2 + (a + \sqrt{z^2 + b^2})^2}}, \quad (8)$$

with mass $M = 1.8 \times 10^{11} M_\odot$, scale length $a = 6$ kpc and scale height $b = 0.3$ kpc. This is a crude approximation to the true potential and one expects to be able to start from a better approximation to the Galaxy’s potential. It is chosen such that the circular speed at the Solar radius is approximately the same as in the true potential, and the scale height is similar to that of the true disc. We chose a scale length that is much greater than that of the true thin disc (which dominates the forces in the solar neighbourhood) as the Miyamoto-Nagai potential falls off quickly with radius, and we want to avoid any risk of having particles at or above the escape speed (at least one action diverges as a particle’s speed tends to the escape speed).

Fig. 8 shows plots of Ω_R against Ω_ϕ (top) and J_R against J_ϕ (bottom). While the clear separation of particles into clumps in both $\mathbf{\Omega}$ and \mathbf{J} seen in Figure 6 is somewhat smeared by using the wrong potential, it is not completely lost. Therefore, even when the true potential is unknown, these plots enable us to identify substructures.

We can go further, and use the displacement of patches in $\mathbf{\Omega}$ space by an erroneous potential to identify the true potential. Specifically, at time t the angle coordinates of the α th particle θ_α satisfy

$$\Omega_\alpha(t - t_0) - (\theta_\alpha - \theta_{\alpha,0}) = 2\pi m_{R,\alpha}, \quad (9)$$

where the particle was at $\theta_{\alpha,0}$ at time t_0 ; the (integer) components of \mathbf{m}_α give the number of oscillations that the particle has made in R, z and ϕ .

There is negligible clumping in θ_z because the satellite’s orbit initially lay in the plane, but at some time t_0 , before the satellite was stripped, individual values of $\theta_{R,\alpha,0}$ were

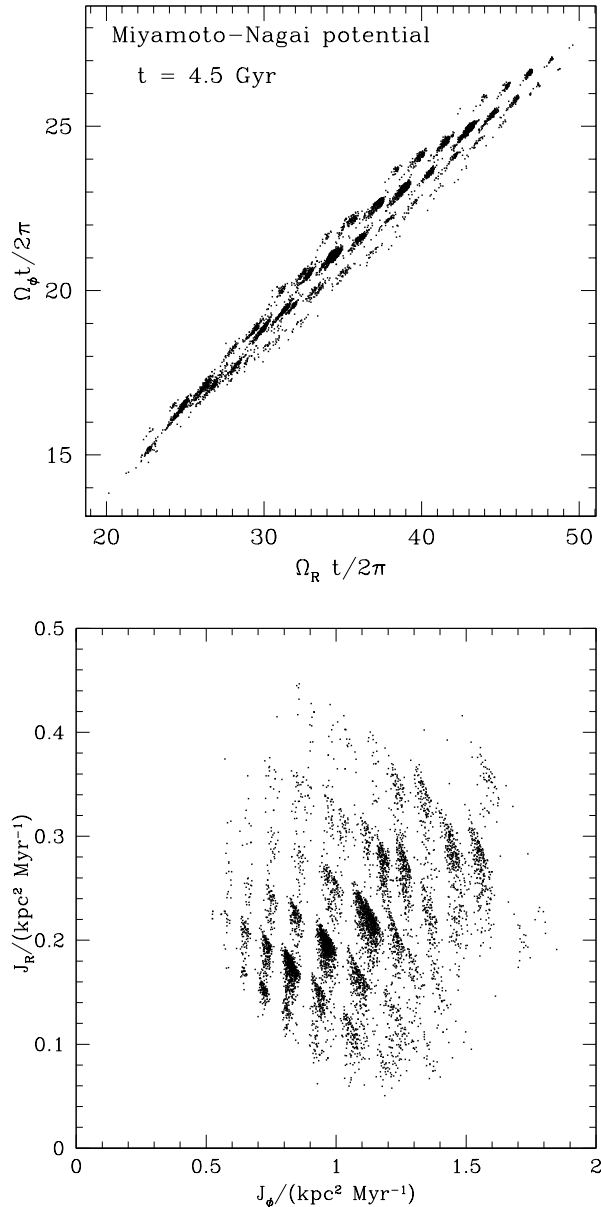


Figure 8. $\Omega_\phi t/2\pi$ (number of azimuthal periods) plotted against $\Omega_R t/2\pi$ (top), and J_R against J_ϕ (bottom) for particles found within 1.5 kpc of the “solar position” in our simulation after 4.5 Gyr as determined in the Miyamoto-Nagai potential described in Section 4.3 (for comparison see the middle panels of Figures 4 & 6).

tightly correlated, as were values of $\theta_{\phi,\alpha,0}$. In fact, in our simulation at $t = 0$, the satellite was centred at $\theta_{\phi,0} = 0$ and at apocentre, where $\theta_R \simeq \pi$ for all orbits. Therefore, we define the statistical measures

$$\begin{aligned} \delta_{R,\alpha} &= \left| \frac{\Omega_{R,\alpha} t' - (\theta_{R,\alpha} - \theta_{R,0}) - 2\pi m_{R,\alpha}}{\pi} \right| \\ \delta_{\phi,\alpha} &= \left| \frac{\Omega_{\phi,\alpha} t' - (\theta_{\phi,\alpha} - \theta_{\phi,0}) - 2\pi m_{\phi,\alpha}}{\pi} \right|, \end{aligned} \quad (10)$$

where the integers $m_{\phi,\alpha}$ and $m_{R,\alpha}$ are chosen such that $\delta_{R,\alpha}$ and $\delta_{\phi,\alpha}$ are minimised; $\theta_{R,0} = \pi$ and $\theta_{\phi,0} = 0$ (in this

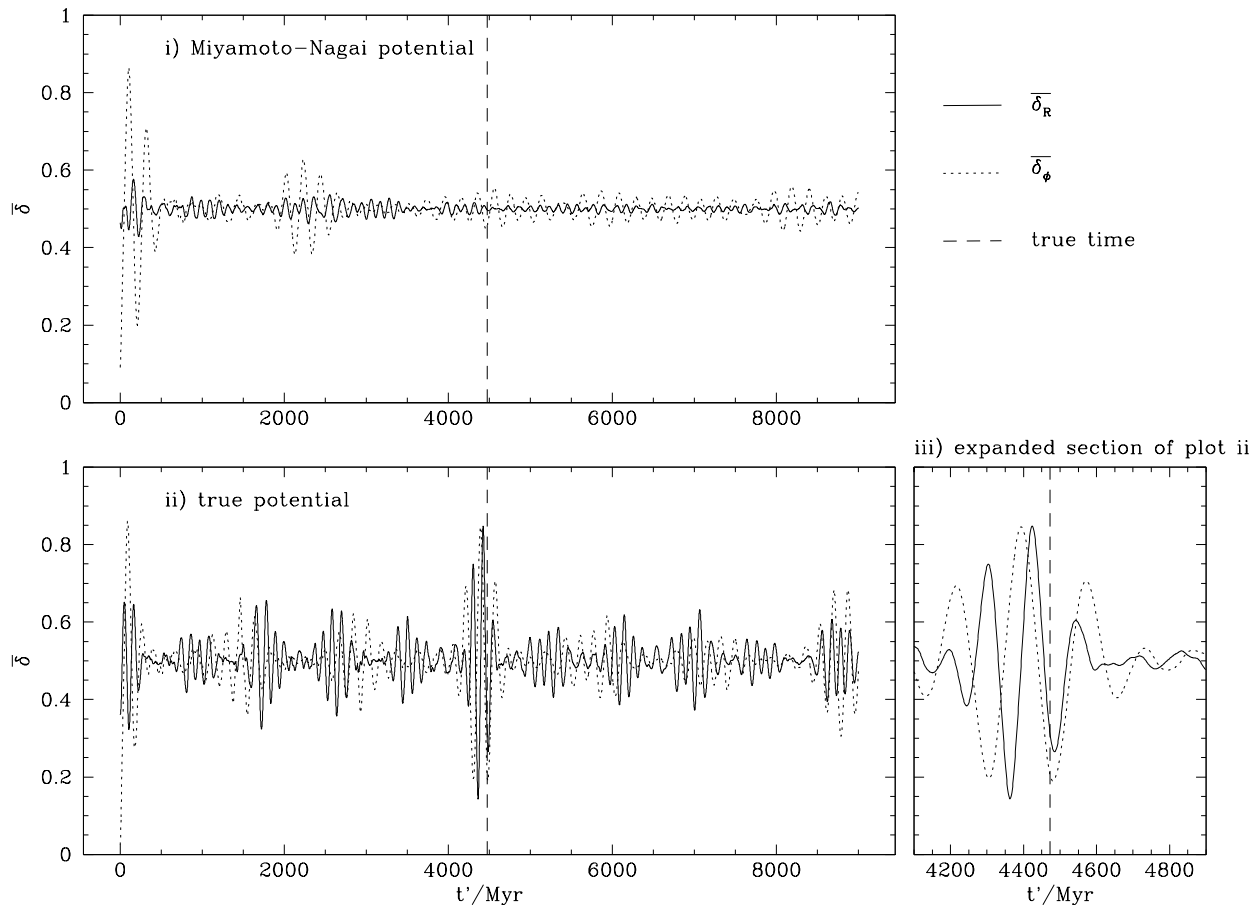


Figure 9. $\bar{\delta}_R$ (solid line), and $\bar{\delta}_\phi$ (dotted line) plotted against t' (see Equation 10); the dashed line indicates the known true value of t . The lower panels (ii & iii) show $\bar{\delta}_R$ and $\bar{\delta}_\phi$ determined using values of Ω and θ found in the same potential that the orbit integration was carried out in – the lower-right panel (iii) being a magnified section of the lower left hand panel (ii), focused around the true value of t . The upper panel (i) shows $\bar{\delta}_R$ and $\bar{\delta}_\phi$ determined using values of Ω and θ found in an incorrect potential (Equation 8). There are strong minima in both $\bar{\delta}_R$ and $\bar{\delta}_\phi$ around the true value of t when the true potential is used, whereas when an incorrect potential is used none is seen.

case) and t' is a free parameter. In these expressions the numerators vary between $\pm\pi$, so when the values of $\Omega_\alpha t'$ are randomly distributed, $\bar{\delta}_i \simeq 0.5$, while when $\Omega_i t'$ has a well defined phase relative to the rest of the numerator, $\bar{\delta}_i$ can approach either zero or 1, depending on whether the two halves of the numerator are in or out of phase with each other.

At $t = 4.5$ Gyr in our simulation $\bar{\delta}_R$ and $\bar{\delta}_\phi$ were evaluated by summing over particles within 1.5 kpc of the Sun. Fig. 9 shows the resulting plots of $\bar{\delta}_R$ and $\bar{\delta}_\phi$ as functions of t' with Ω_α and θ_α determined in the Miyamoto-Nagai potential (upper panel) and in the true potential (lower panel). The upper panel shows that when the dynamical variables are evaluated in an erroneous potential, the $\bar{\delta}_i$ scarcely move from their mean values after the first few megayears, and when one of them does move downwards, the other does not. By contrast in the lower panel for the true potential both $\bar{\delta}_i$ display sustained beats as the relative phases of the two terms that make up the numerators in equations (10) have stable relative phases. In the neighbourhood of the true

disruption time of the relic the beating swells in amplitude and, as the exploded view on the right of the figure shows, both move down together just 10 Myr past the relic's true age.

When applying the test involving the $\bar{\delta}_i$ to real observational data, it will be necessary to search for beats over both t' and the mean of the initial azimuthal phases $\theta_{\phi,\alpha}$. Hence, Fig. 9 oversimplifies the problem because it shows a one-dimensional search rather than a two-dimensional one. Moreover, if the satellite was initially on an inclined orbit rather than one in the plane, the vertical angles θ_z would be involved, so coincident beats would be required in three angle-dependent variables $\bar{\delta}_i$ rather than two. Consequently, a smaller fraction of a relic's stars would satisfy this condition at a given time, making it harder to identify a relic against background noise. The upside of the involvement of θ_z is that it would give us the opportunity to constrain the vertical structure of the potential; a relic of a satellite that started from $J_z \simeq 0$ only probes the Galactic rotation curve.

Real data will also have background stars that did not

come from the satellite. Naturally, the Poisson noise in the distribution of background stars makes it harder to identify overdensities in \mathbf{J} -space, but once the overdensities associated with a remnant have been identified, background stars have negligible impact on the ability of the $\bar{\delta}_i$ to determine the disruption time: any star in the overdensity is in the same part of Ω -space as the remnant's stars, so the contributions to equation (10) from background and remnant stars will differ only in the relevant values of θ . These differences will inevitably be small because we are dealing with a small survey volume. For example, if 20% of the stars identified as being part of the remnant are actually background stars, and are – on average – displaced from the position on the orbit where a typical remnant member with the same Ω would be by $\Delta\theta_i = 0.2$ (equivalent to ~ 1.5 kpc in the ϕ -direction), this would only make a difference of 0.01 to $\bar{\delta}_i$.

Before the satellite is completely disrupted, it is affected by dynamical friction, which will cause spreading in velocity space. However this is a significantly smaller effect than that due to the self gravity and initial velocity dispersion in the satellite for an object of this mass – the Chandrasekhar dynamical friction formula (e.g. Binney & Tremaine 2008, §8.1) suggests that a satellite of this mass should be decelerated by $\sim 10 \text{ km s}^{-1} \text{ Gyr}^{-1}$, and this decreases in direct proportion to the satellite mass as it is stripped. Hence including dynamical friction would shift individual velocities by significantly less than their intrinsic scatter, namely the internal velocity distribution of the satellite (18.6 km s^{-1}).

These matters, and any others that arise, will be investigated further, but Fig. 9 clearly conveys the essential idea and gives a tantalising taste of the diagnostic potential of angle variables.

5 SECULAR EVOLUTION

Stars have continued to form at a significant rate throughout the lifetime of the Galaxy's thin disc, and it must be presumed that the disc's mass has increased significantly over the last 5 Gyr. Since actions are adiabatic invariants, such secular evolution of the Galactic potential does not affect the distribution of relic stars in the $J_\phi - J_R$ plane (Fig. 5). Secular evolution causes the frequencies at fixed \mathbf{J} to become explicit functions of time, so we should write $\Omega(\mathbf{J}, t)$, and the increment in θ_i over time t changes from $\Delta\theta_i = \Omega_i t$ to $\Delta\theta_i = \int_0^t dt \Omega_i$. The conditions for a relic star to be in the solar neighbourhood are given values of $\Delta\theta_i \bmod 2\pi$ for $i = R, \phi$. Since with secular evolution $\Delta\theta_i$ remains a continuous function of \mathbf{J} , these conditions continue to be satisfied only in a grid of patches in action space; secular evolution shifts the patches, but does not blur them. Hence the diagnostic power of plots like Fig. 6 is unaffected by secular evolution.

In the presence of secular evolution it becomes necessary in equation (9) to replace $\Omega_\alpha(t-t_0)$ by $\int_{t_0}^t dt \Omega_\alpha$. To evaluate the required integrals, one must adopt a model of the history of the potential, which determines the time dependence of Ω . The required model is self-evident if secular evolution is confined to growth in the disc's mass at a known rate. Uncertainties in this rate will make it harder to locate beats in Fig. 9.

Of course the key to calculating the secular evolution of stellar systems, be they globular clusters or galaxies, is to express their distribution functions in terms of actions (e.g. Sellwood & McGaugh 2005), so the availability of orbital tori for arbitrary potentials opens up new horizons in this area.

6 SUMMARY

A major hope of “near-field cosmology” is to identify within the Galaxy groups of stars that were accreted together (Freeman & Bland-Hawthorn 2002). We have demonstrated the power of angle-action coordinates for doing this by studying the debris of a self-gravitating satellite of mass $3.75 \times 10^8 M_\odot$, released within the plane of a realistic Galactic potential on an orbit with apocentre at 9 kpc. On this short-period orbit the satellite's stars become well phase mixed within a couple of gigayears, and they are quite widely distributed in action space. Nonetheless, the stars that lie within 1.5 kpc of the Sun are concentrated into a grid of patches in action space because only stars with certain frequencies are currently near the Sun. To see the patchiness of the distribution in action space it is not necessary to use the angle-action coordinates of the true Galactic potential. But the correct potential must be used if statistical measures constructed from the angle coordinates of stars are to show a characteristic pattern of beats from which the time at which the relic was disrupted can be deduced. Hence our results suggest a two-stage procedure: first a reasonable approximation to the Galactic potential is used to identify relics through the clustering of their stars' points around the nodes of a grid in action space. Then once a relic has been identified, the Galactic potential would be adjusted until the angle-variable diagnostics showed pronounced beats. This second step would not only pin down the Galaxy's potential, but also reveal the time at which relic was disrupted.

Growth in the mass of the disc since the satellite fell in would have significant effects only on Fig. 9: to recover this plot it would be necessary to model the time dependence of the Galactic potential, so that the integrals $\int dt \Omega$ could be evaluated. We anticipate that with the help of angle-action coordinates this could be done to sufficient accuracy, but defer this refinement to a subsequent publication.

We have neglected the deviations of the Galactic potential from axisymmetry. Could these deviations have a significant impact? Jurić et al. (2008) use star counts in the SDSS survey to show that the Galaxy's thick disc is remarkably axisymmetric near the Sun. This finding suggests that it is legitimate to neglect the bar when searching for relics within the thick disc, such as the Arcturus group. In general, the quadrupole moments of the bar's gravitational potential will decline rapidly outside the end of the bar at $R \sim 3$ kpc, so stars that are not resonant with the bar will not be strongly affected by it. The observed axisymmetry of the thick disc suggests that few if any of its stars are resonantly trapped by the bar, so their orbits can be safely modelled with an axisymmetric potential. The question of how the – phase-dependent – effects of the bar would impact Fig. 9 may prove important.

The exciting possibilities discussed here rest on two foundations. One is the availability of angle-action coordi-

nates for any given potential, and the other is the availability of full phase space coordinates for significant samples of stars. The torus construction technique developed in a series of papers starting with McGill & Binney (1990) can provide angle-action coordinates, and programmes such as the Geneva-Copenhagen, RAVE and Gaia surveys will provide the phase space coordinates.

Currently the torus technique is restricted to either axisymmetric systems or two-dimensional non-rotating bars. However, extension to three-dimensional bars, including bars that are rotating with a constant pattern speed, is in principle straightforward and will be attempted soon.

Clearly when this technique is used to search a real catalogue for relics, and then to analyse them, difficulties will be encountered that we have ignored here. Most obviously one will have to contend with errors in the phase space coordinates of stars (primarily due to errors in distances) and with the difficulty in picking out overdensities in action space against a background of Poisson noise from field stars. We are currently applying the method to $\sim 200\,000$ stars from the RAVE survey and hope to report the results in the near future.

ACKNOWLEDGMENTS

We are grateful to Walter Dehnen for making his torus code available to us. We also thank Ben Burnett, John Magorrian and Andy Eyre and the other members of the Oxford dynamics group for critical comments on this work. PJM is supported by a grant from the Science and Technology Facilities Council.

REFERENCES

- Abadi M. G., Navarro J. F., Steinmetz M., Eke V. R., 2003, *ApJ*, 597, 21
- Belokurov V., Zucker D. B., Evans N. W., Gilmore G., Vidrih S., Bramich D. M., Newberg H. J., Wyse R. F. G., Irwin M. J., Fellhauer M., Hewett P. C., Walton N. A., Wilkinson M. I., Cole N., Yanny B., Rockosi C. M., Beers T. C., Bell E. F., Brinkmann J., Ivezić Ž., Lupton R., 2006, *ApJL*, 642, L137
- Binney J., Tremaine S., 2008, *Galactic dynamics*. Princeton, NJ, Princeton University Press
- Chereul E., Crézé M., Bienaymé O., 1999, *A&AS*, 135, 5
- Dehnen W., 1999, *ApJL*, 524, L35
- , 2000, *AJ*, 119, 800
- , 2002, *Journal of Computational Physics*, 179, 27
- Dehnen W., Binney J., 1998, *MNRAS*, 294, 429
- Eggen O. J., 1971, *PASP*, 83, 271
- Famaey B., Jorissen A., Luri X., Mayor M., Udry S., Dejonghe H., Turon C., 2005, *A&A*, 430, 165
- Freeman K., Bland-Hawthorn J., 2002, *AnnRA&A*, 40, 487
- Fux R., 2001, *A&A*, 373, 511
- Helmi A., de Zeeuw P. T., 2000, *MNRAS*, 319, 657
- Helmi A., Navarro J. F., Nordström B., Holmberg J., Abadi M. G., Steinmetz M., 2006, *MNRAS*, 365, 1309
- Helmi A., White S. D. M., 1999, *MNRAS*, 307, 495
- Helmi A., White S. D. M., de Zeeuw P. T., Zhao H., 1999, *Nat*, 402, 53
- Helmi A., White S. D. M., Springel V., 2003, *MNRAS*, 339, 834
- Ibata R. A., Gilmore G., Irwin M. J., 1994, *Nat*, 370, 194
- Jurić M., Ivezić Ž., Brooks A., Lupton R. H., Schlegel D., Finkbeiner D., Padmanabhan N., Bond N., Sesar B., Rockosi C. M., Knapp G. R., Gunn J. E., Sumi T., Schneider D. P., Barentine J. C., Brewington H. J., Brinkmann J., 2008, *ApJ*, 673, 864
- Kaasalainen M., Binney J., 1994, *MNRAS*, 268, 1033
- Lynden-Bell D., Lynden-Bell R. M., 1995, *MNRAS*, 275, 429
- McGill C., Binney J., 1990, *MNRAS*, 244, 634
- Navarro J. F., Helmi A., Freeman K. C., 2004, *ApJL*, 601, L43
- Nordström B., Mayor M., Andersen J., Holmberg J., Pont F., Jørgensen B. R., Olsen E. H., Udry S., Mowlavi N., 2004, *A&A*, 418, 989
- Perryman M. A. C., de Boer K. S., Gilmore G., Høg E., Lattanzi M. G., Lindgren L., Luri X., Mignard F., Pace O., de Zeeuw P. T., 2001, *A&A*, 369, 339
- Press W. H., Flannery B. P., Teukolsky S. A., 1986, *Numerical recipes. The art of scientific computing*. Cambridge: University Press
- Sellwood J. A., McGaugh S. S., 2005, *ApJ*, 634, 70
- Springel V., Hernquist L., 2003, *MNRAS*, 339, 289
- Steinmetz M., Zwitter T., Siebert A., Watson F. G., Freeman K. C., Munari U., Campbell R., Williams M., Seabroke G. M., Wyse R. F. G., Parker Q. A., Bienaymé O., Roeser S., Gibson B. K., Gilmore G., Grebel E. K., Helmi A., Navarro J. F., Burton D., Cass C. J. P., Dawe J. A., Fiegert K., Hartley M., Russell K. S., Saunders W., Enke H., Bailin J., Binney J., Bland-Hawthorn J., Boeche C., Dehnen W., Eisenstein D. J., Evans N. W., Fiorucci M., Fulbright J. P., Gerhard O., Jauregi U., Kelz A., Mijović L., Minchev I., Parmentier G., Peñarrubia J., Quillen A. C., Read M. A., Ruchti G., Scholz R.-D., Siviero A., Smith M. C., Sordo R., Veltz L., Vidrih S., von Berlepsch R., Boyle B. J., Schilbach E., 2006, *AJ*, 132, 1645
- Tremaine S., 1999, *MNRAS*, 307, 877
- White S. D. M., Rees M. J., 1978, *MNRAS*, 183, 341
- Zwitter T., Siebert A., Munari U., Freeman K. C., Siviero A., Watson F. G., Fulbright J. P., Wyse R. F. G., Campbell R., Seabroke G. M., Williams M., Steinmetz M., Bienaymé O., Gilmore G., Grebel E. K., Helmi A., Navarro J. F., Anguiano B., Boeche C., Burton D., Cass P., Dawe J., Fiegert K., Hartley M., Russell K., Veltz L., Bailin J., Binney J., Bland-Hawthorn J., Brown A., Dehnen W., Evans N. W., Re Fiorentin P., Fiorucci M., Gerhard O., Gibson B., Kelz A., Kujken K., Matijević G., Minchev I., Parker Q. A., Peñarrubia J., Quillen A., Read M. A., Reid W., Roeser S., Ruchti G., Scholz R.-D., Smith M. C., Sordo R., Tolstoj E., Tomasella L., Vidrih S., de Boer E. W., 2008, *AJ*, 136, 421